

RSC Advances



This is an *Accepted Manuscript*, which has been through the Royal Society of Chemistry peer review process and has been accepted for publication.

Accepted Manuscripts are published online shortly after acceptance, before technical editing, formatting and proof reading. Using this free service, authors can make their results available to the community, in citable form, before we publish the edited article. This *Accepted Manuscript* will be replaced by the edited, formatted and paginated article as soon as this is available.

You can find more information about *Accepted Manuscripts* in the [Information for Authors](#).

Please note that technical editing may introduce minor changes to the text and/or graphics, which may alter content. The journal's standard [Terms & Conditions](#) and the [Ethical guidelines](#) still apply. In no event shall the Royal Society of Chemistry be held responsible for any errors or omissions in this *Accepted Manuscript* or any consequences arising from the use of any information it contains.

Nano-granular Sn impregnated NiTi alloy matrix anode for high voltage Li-ion pouch cells

P. Manikandan^a, P. Periasamy^{a*} and R. Jagannathan^{b*}

^aLithium Batteries - Electrochemical Power Sources Division, ^bFunctional Materials Division
CSIR - Central Electrochemical Research Institute, Karaikudi – 630 006, Tamilnadu, India

*Correspondence: jags57_99@yahoo.com, Tel: +919487167780, Fax: +914565227713;
periasamylibatt@gmail.com, Tel: +914565241421, Fax: +914565227713.

Abstract

Well characterized nano-granular Sn impregnated inactive NiTi alloy matrix has been synthesized through a viable and facile *mill-heat* method as suitable anode matrix for Li-ion batteries. These poly crystalline grains of Sn in NiTi alloy matrix exhibit an average size of ~ 25 nm. Distinct advantages of Sn active site(s) hosting intercalated Li species are better electronic properties, favorable elastic features in particular Poisson ratio akin to Sn-NiTi matrix and cycling stability facilitating EV, HEV applications. The optimum anode composition Sn_{0.70}Ni_{0.20}Ti_{0.10} alloy matrix vs LNi_{1/3}Mn_{1/3}Co_{1/3}O₂:LNi_{0.5}Mn_{0.5}O₂ composite cathode (wt. % of 75:25) when used in the rolling in smart-design Li-ion pouch cell fabricated in the lab yields high voltage (> 4.2 V) along with the demonstration of running a toy-car with a load 1.1 Wh on a coarse bitumen road.

Keywords: Alloy matrix anode; Poisson ratio; Intercalation; Smart-design; Li-ion pouch cell.

1. Introduction

Since the introduction of first electrochemical power sources based applications, Li-ion battery community¹⁻³ has been endeavoring to realize optimum performance in terms of cell capacity, voltage, structural/cycling stability and safety aspects eventually meriting applications in electric vehicles (EVs) and hybrid electric vehicles (HEVs) through judicious choice/combination of anode and cathode systems.^{1,4-5} In the last two decades, intense research on cathode materials has culminated in composite cathode system yielding impressive

electrochemical performance ($> 230 \text{ mAh g}^{-1}$)⁶⁻⁸ replacing the celebrated LiCoO_2 material.⁹⁻¹³ In spite of the remarkable success achieved, incompatibility of the graphite anode *viz.*, pronounced structural instability of lithiated graphite during (de)intercalation process is a challenging task deserving importance. This makes imperative intense research on appropriate anode system to realize complete exploitation of the improved Li-ion cell performance.

There are numerous reports on anode research based on $\text{Li}_4\text{Ti}_5\text{O}_{12}$,¹⁴ TiO_2 ¹⁵ and Co_3O_4 ,¹⁶ anode systems. However, undesirable high working voltage and low theoretical capacity of these systems make them unsuitable anode systems for applications.¹⁴⁻¹⁵ Although these shortcomings can be partly overcome with the choice of alloy anode systems *viz.*, Si-M-C and Sn-M-C carbonaceous composite alloy anodes (M= Fe, Sb, Ni, Co, M is an inactive metal element to Li).¹⁷⁻²⁵ The concept of composite alloy anode systems based on active/inactive nano composite concept with carbon anode system has gained importance for applications in electronic devices but not in EVs and HEVs owing to imminent Li trapping in the amorphous carbon and solid electrolyte interface (SEI) formation on the carbon surface.²²⁻³⁰ The inherent poor scope for flexibility (to accommodate Li^+ ions during cycling required) of the carbon paved way for other appropriately inactive systems based on inactive NiTi matrix such as Si-NiTi³¹ and Sn-NiTi³²⁻³³ alloy matrix anode to improve the cycling performance. In this context, it is important to take note of reports employing Si as active site for accommodating intercalated Li^+ ions with scope for volume expansion with NiTi alloy matrix as inactive base.³¹ However, there are many aspects weighing against the use of non-metallic Si as active site in the anode composition *viz.*, unduly large volume expansion ($> 300\%$ than Sn), low electrical resistivity (Si - $2.52\text{E}^{-12} \text{ M}\Omega \text{ cm}^{-1}$ compared with Sn - $0.0917 \text{ M}\Omega \text{ cm}^{-1}$) and also poor semi-conductive charge transportation ($10^{-5} \text{ S cm}^{-1}$ compared with graphite 10^3 S cm^{-1} and Sn) eventually hindering the electronic diffusion

in the electrode redox process.³⁴ Also, other significant advantages of using Sn over Si which should be considered in the full cell design are: better electrical contact over cycling, higher thin coating during electrode fabrication and reasonable cycling stability suitable for EVs and HEVs application. The capacity loss can be contained by averting the irreversible reactions with the choice of an inactive NiTi matrix to Li and electrolyte during cycling. In view of this, the replacement of carbon through Sn alloyed with NiTi alloy matrix is more favorable to Si and also in terms of higher Poisson's ratio (ν).³⁵⁻³⁶ Close matching of the elastic properties in particular Poisson's ratio of Sn ($\nu_{\text{Sn}} = 0.33$) with NiTi alloy matrix system ($\nu_{\text{Ni}} = 0.3$, $\nu_{\text{Ti}} = 0.305$) suggests a clear advantage in terms of flexibility to accommodate Li^+ ions during cycling in contrast to Si ($\nu_{\text{Si}} = 0.17$) based system having only half of the NiTi ($\nu_{\text{Ni}} = 0.3$, $\nu_{\text{Ti}} = 0.305$) alloy matrix. Unique advantage of NiTi matrix exhibiting super-elasticity characteristics facilitating resilience to absorb large stress coming from the large volume expansion of Sn and also affording excellent electrical contact between the active material and the current collector during cycling.³¹⁻³³ It is pertinent to note that Sn having ample scope for volume expansion during cycling to accommodate Li^+ ions during (de)intercalation process has clear advantage to ensure structural stability coupled with superior electrochemical performance.

These points in mind serving as the motivation of the present investigation, a more feasible Sn alloyed with NiTi inactive matrix anode synthesized through a simple mill-heat process is proposed in this work. Also, major daunting challenge concerning the design of Li-ion batteries is unduly heavy metallic cell casings which when piled-up in large numbers limit the scope for application in devices such as EVs and HEVs. The issue of heavy casings can be overcome through alternative design based on aluminum pouches.³⁷ In this scenario, the design of Li-ion batteries on high voltage energy storage system *viz.*, Li-ion pouch cell fabricated with

the $\text{Sn}_{0.70}\text{Ni}_{0.20}\text{Ti}_{0.10}$ (Sn-NiTi) alloy matrix anode vs $\text{LNi}_{1/3}\text{Mn}_{1/3}\text{Co}_{1/3}\text{O}_2:\text{LNi}_{0.5}\text{Mn}_{0.5}\text{O}_2$ (wt. % of 75:25) composite cathode material³⁸ for high voltage (> 4.2 V) Lithium-ion batteries are presented in detail.

2. Experimental aspects

In the present investigation, Sn-NiTi alloy matrix anode has been synthesized through a facile mill-heat process comprising two steps. (i) high energy wet ball milling of Sn, Ni and Ti metal powders followed by (ii) high temperature calcination of this blend in an argon atmosphere and the composition of the anode has been optimized. Required amounts (weight %) of Sn (–100 mesh, 99.85%, metal basis, Alfa Aesar), Ni (100 mesh, 99.5%, S D Fine) and Ti (98.5%, Himedia) metal powders were mixed together and high energy wet ball milled for 50 h (in toluene medium) using FRITSCH pulverisette 7 pulverizer at 500 rpm followed by heating at 900 °C for 5 h in Ar atmosphere. In this work following alloy matrix having compositions (with relative wt. %) have been tried: 60:25:15 ($\text{Sn}_{0.60}\text{Ni}_{0.25}\text{Ti}_{0.15}$); 70:20:10 ($\text{Sn}_{0.70}\text{Ni}_{0.20}\text{Ti}_{0.10}$); 80:15:05 ($\text{Sn}_{0.80}\text{Ni}_{0.15}\text{Ti}_{0.05}$) and 100:00:00 ($\text{Sn}_{1.00}\text{Ni}_{0.00}\text{Ti}_{0.00}$) as representative examples (Fig. 1). In these trials, the latter two compositions with higher Sn content were not used in the further study for the reason that the homogeneous alloy formation was not observed in these samples due to the pronounced segregation of Sn particles (Fig. 1c, d).

Phase formations of these alloy matrix samples *viz.*, $\text{Sn}_{0.60}\text{Ni}_{0.25}\text{Ti}_{0.15}$ (SnNiTi), $\text{Sn}_{0.70}\text{Ni}_{0.20}\text{Ti}_{0.10}$ (Sn-NiTi) have been ascertained through powder X-ray diffraction (XRD) studies using a Bruker D8 Advance X-ray diffractometer with a Cu $K\alpha$ X-ray source ($\lambda=1.5418$ Å, with corundum Al_2O_3 as the internal standard) and the measurements were recorded in the 2θ range 10 – 80°. During crystallite size estimate for these granular samples has been made using Debye-Scherrer formula with the consideration of XRD line width data. Particle morphologies of

the alloy matrix samples *viz.*, $\text{Sn}_{0.60}\text{Ni}_{0.25}\text{Ti}_{0.15}$, $\text{Sn}_{0.70}\text{Ni}_{0.20}\text{Ti}_{0.10}$ were analyzed through field-emission scanning electron microscopy (FE-SEM) MODEL ZEISS SUPRATM 55VP and also transmission electron microscope (TEM) Hitachi S-3000H. The corresponding selected area electron diffraction patterns (SAED) of the SnNiTi and Sn-NiTi alloy matrix samples have also been recorded. In order to have insights on relative compositions of these elements (Sn:Ni:Ti), elemental mapping studies have been made using FE-SEM based on energy dispersive X-ray analysis.

Concerning electrochemical characterization of these samples, cyclic voltammograms (CV) were recorded at a scan rate of 0.1 mV s^{-1} in the voltage range 0.005 to 2.4 V under CR2032 cell configuration using VMP3Z (Biological) Multi-Channel Potentiostat/Galvanostat electrochemical workstation. Charge-discharge galvanostatic studies were carried out in the voltage range of 0.005 - 2 V using Arbin multichannel cycler instrument (BT2000). Coin cells corresponding to test cell were assembled using lithium foil (thickness: 0.75 mm) and as-synthesized Sn-NiTi alloy matrix sample coated on Cu foil as current collector. Also, Li-ion pouch cell with Celgard[®] 2340 separator (rolling in smart-design) has been fabricated using a double side coated Sn-NiTi alloy matrix negative electrode and composite positive electrode enclosed a laminated pouch. In this trial, active materials of the negative and positive electrodes used were having the typical composition of $\text{Sn}_{0.70}\text{Ni}_{0.20}\text{Ti}_{0.10}$ and $\text{LNi}_{1/3}\text{Mn}_{1/3}\text{Co}_{1/3}\text{O}_2:\text{LNi}_{0.5}\text{Mn}_{0.5}\text{O}_2$ (wt. % 75:25) respectively along with 1 M solution of LiPF_6 in 1:1 (v/v) EC-DMC mixture was used as the electrolyte. The synthesis details of the composite cathode materials used in this study is the same as described earlier.³⁸

Turning to the describe the fabrication of Li-ion pouch cell through rolling in smart-design: crucial design parameters are double sided electrode having width, length, thickness

(with current collector) and weight of the anode/cathode 5 cm, 25 cm, $\sim 135/143 \mu$ and 1.8/3.7 g for the compositions $\text{Sn}_{0.70}\text{Ni}_{0.20}\text{Ti}_{0.10}$ and $\text{LNi}_{1/3}\text{Mn}_{1/3}\text{Co}_{1/3}\text{O}_2:\text{LNi}_{0.5}\text{Mn}_{0.5}\text{O}_2$. Furthermore, the cathode was fabricated using a doctor blade-coating slurry of 80% $\text{LNi}_{1/3}\text{Mn}_{1/3}\text{Co}_{1/3}\text{O}_2:\text{LNi}_{0.5}\text{Mn}_{0.5}\text{O}_2$, 15% SP-carbon (Timcal) and 5% PVdF in NMP coated over aluminum foil (15 μm). The anode was fabricated using 80% $\text{Sn}_{0.70}\text{Ni}_{0.20}\text{Ti}_{0.10}$, 15% SP-carbon (Timcal) and 5% PVdF in NMP slurry coated over copper foil (9 μm) and dried at 85 °C for 12 h in a vacuum oven. The area, thickness and weight of the as-synthesized alloy matrix electrodes were 1.54 cm^2 , $\sim 68 \mu$ (with current collector) and 6.16 mg for the active material (SnNiTi) under CR2032 cell configuration. Both coin and pouch cells were assembled in an argon-filled glove box (mBRAUN MB200G) with oxygen and moisture levels less than 0.1 ppm. The electrochemical performance of the thus fabricated Li-ion pouch cell has been investigated in terms of charge-discharge studies and also demonstration of its application in kits such as electronic toy-car.

3. Results and discussion

Clear advantage of Sn-NiTi alloy matrix as anode³²⁻³³ paves way for its application in EVs and HEVs. With the set goal of synthesizing this anode through a more feasible and controllable physicochemical route, we propose a facile mill-heat process, although there are reports on the synthesis of Sn-NiTi alloy matrix.³²⁻³³ Details on the characterization of the anode system has been can be outlined in the following:

3.1. XRD analysis of Sn nano-grain impregnated into NiTi alloy matrix

Chemical phase analysis based on powder XRD patterns can generate vital clues on the phase formation-segregation, integration of alloy constituents for eventual optimization of anode performance. It can be seen from Fig. 2 that the diffraction patterns of $\text{Sn}_{0.60}\text{Ni}_{0.25}\text{Ti}_{0.15}$ and

$\text{Sn}_{0.70}\text{Ni}_{0.20}\text{Ti}_{0.10}$ compositions can be well matched with both the tetragonal Sn (JCPDS# 00-04-0673) and also crystalline Sn in the NiTi alloy matrix (JCPDS# 03-065-0991) phases.³²⁻³³ However, the relative intensities of these lines have profound dependence on Sn content in the alloy composition. In the case of $\text{Sn}_{0.70}\text{Ni}_{0.20}\text{Ti}_{0.10}$ alloy matrix, the obvious peaks observed at 30.8, 32.1, 44 and 45° (2 θ) can be assigned to tetragonal Sn, suggesting presence of Sn in the inactive NiTi alloy matrix (indicated using red * mark).³²⁻³³ Additional peaks observed at 26.1, 30.5 and 42.7° can be attributed to the formation of SnNiTi alloy matrix as indicated using rose colored * mark in Fig. 2.³²⁻³³ But, for the composition having $\text{Sn}_{0.60}\text{Ni}_{0.25}\text{Ti}_{0.15}$, the presence of crystalline Sn is less in the NiTi alloy matrix compared with $\text{Sn}_{0.70}\text{Ni}_{0.20}\text{Ti}_{0.10}$ composition. Also, crystallite size estimated using Debye-Scherrer XRD line broadening data for the alloy matrix indicated a value of $\Phi_{\text{ave}} = 76$ nm and 115 nm for $\text{Sn}_{0.60}\text{Ni}_{0.25}\text{Ti}_{0.15}$ and $\text{Sn}_{0.70}\text{Ni}_{0.20}\text{Ti}_{0.10}$ respectively. Furthermore, X-ray diffraction patterns of these $\text{Sn}_{0.60}\text{Ni}_{0.25}\text{Ti}_{0.15}$ and $\text{Sn}_{0.70}\text{Ni}_{0.20}\text{Ti}_{0.10}$ compositions show some more peaks of lower intensity which may correspond to the Ni_3Sn_4 intermetallic phase (JCPDS# 00-04-0845, blue * mark) resulting from the prolonged milling followed by a part of Sn reacted with Ni during calcination.³³ Also, there are no additional detectable peaks corresponding to the intermetallic phases *viz.*, Sn-Ni, Sn-Ti and Ni-Ti in line with earlier reports.³²⁻³³

It turns out that on closer examination of the XRD pattern of the sample with composition $\text{Sn}_{0.60}\text{Ni}_{0.25}\text{Ti}_{0.15}$ yields a pattern showing perfect match with that of SnNiTi alloy both in terms of d spacing and relative intensity pattern. This readily indicates the complete integration of nano-grains of Sn in to the NiTi base and hence the formation of SnNiTi alloy whilst the composition $\text{Sn}_{0.70}\text{Ni}_{0.20}\text{Ti}_{0.10}$ leads to interesting results. In this situation, the XRD pattern lines match well with both the tetragonal Sn (JCPDS# 00-04-0673) and also crystalline

Sn in the NiTi alloy inactive base matrix (JCPDS# 03-065-0991). Indeed, this is the most desirable physicochemical phase condition yielding optimum electrochemical results. Of the two anode compositions $\text{Sn}_{0.60}\text{Ni}_{0.25}\text{Ti}_{0.15}$ and $\text{Sn}_{0.70}\text{Ni}_{0.20}\text{Ti}_{0.10}$ investigated, the former composition leads to complete SnNiTi alloy formation which is not at all preferred for the optimal electrochemical performance. On the other hand the latter composition results in the formation of preferred nano-grain Sn impregnated into NiTi inactive alloy matrix. It is pertinent to mention that nano-grains of Sn impregnated into the inactive alloy base serve as active sites for (de)intercalation thus explaining good electrochemical performance realized in this system.³²⁻³³ Indeed, results of the present investigation also have confirmed this hypothesis.

3.2. Morphological and microstructure features using FE-SEM, TEM and SAED studies

It is established that morphology and microstructure features of both cathode and anode nano particles play a crucial role in determining the electrochemical performance of Li-ion batteries.³⁹ Inspection of FE-SEM micrograph (Fig. 3) of samples with compositions $\text{Sn}_{0.60}\text{Ni}_{0.25}\text{Ti}_{0.15}$ and $\text{Sn}_{0.70}\text{Ni}_{0.20}\text{Ti}_{0.10}$, we have that the former exhibits a spongy product with pronounced agglomeration lacking clear definition of particle morphology (Fig. 3a) while the latter results in Sn impregnated, defined granular fine particles of size < 50 nm (Fig. 3b) warranting closer examination at higher magnification using TEM coupled with SAED analysis.

From the TEM images, it can be confirmed that $\text{Sn}_{0.60}\text{Ni}_{0.25}\text{Ti}_{0.15}$ again leads to highly agglomerated spongy morphology (Fig. 4a,b) while the second sample having the composition $\text{Sn}_{0.70}\text{Ni}_{0.20}\text{Ti}_{0.10}$ invariably leads to impregnated fine particles of disparate morphologies (Fig. 4d,e).³¹⁻³³ Closer examination of Fig. 4e reveals occurrence of dark polyhedral grains distributed over spongy gray matrix background. Apparently, this might suggest distribution of Sn particles over inactive NiTi alloy matrix.³¹⁻³³ Results of the SAED patterns are consistent with this

hypothesis. That is, the scope for occurrence of free standing nano-grains Sn impregnated into the inactive NiTi alloy matrix seems to be more pronounced as revealed from brighter spotty SAED rings (Fig. 4f) in $\text{Sn}_{0.70}\text{Ni}_{0.20}\text{Ti}_{0.10}$ system is more dominant to account for better electrochemical performance over $\text{Sn}_{0.60}\text{Ni}_{0.25}\text{Ti}_{0.15}$ (Fig. 4c). Furthermore, clear quantitative insights on relative individual elemental constituent of these two alloy matrix samples at the given spot become possible with the FE-SEM elemental mapping images supported with energy dispersive X-ray analysis data *viz.*, $\text{Sn}_{0.60}\text{Ni}_{0.25}\text{Ti}_{0.15}$ (Fig. 5) and $\text{Sn}_{0.70}\text{Ni}_{0.20}\text{Ti}_{0.10}$ (Fig. 6).

3.3. CV results of SnNiTi/nano-granular Sn in NiTi alloy matrices

CV studies have been carried out for these Li cells (Li vs $\text{Sn}_{0.60}\text{Ni}_{0.25}\text{Ti}_{0.15}$ and Li vs $\text{Sn}_{0.70}\text{Ni}_{0.20}\text{Ti}_{0.10}$) at a scan rate of 0.1 mV s^{-1} in the voltage range 0.005 to 2.4 V as depicted in Fig. 7. From these results, it can be seen that the peak position of the Sn-NiTi alloy matrix for five cycles remains constant and corresponds to that of pure Sn electrode consistent with earlier reports.^{21,32,40} Obviously, the presence of cathodic peaks (Li vs $\text{Sn}_{0.60}\text{Ni}_{0.25}\text{Ti}_{0.15}$ / Li vs $\text{Sn}_{0.70}\text{Ni}_{0.20}\text{Ti}_{0.10}$) at 0.62/0.57, 0.45/0.44 and 0.26/0.25 V can be attributed to Li intercalation into the nano-grains of Sn forming different Li-Sn alloy phase(s) while the peaks at 0.64, 0.74 and 0.80 V for the deintercalation of the Li from Li-Sn phase(s).^{21,32,40} In view of these results, the nano-grains of Sn are expected to be predominant active phase for the Li in the SnNiTi and Sn-NiTi alloy matrices. Also comparing the CV results of SnNiTi ($\text{Sn}_{0.60}\text{Ni}_{0.25}\text{Ti}_{0.15}$) and Sn-NiTi ($\text{Sn}_{0.70}\text{Ni}_{0.20}\text{Ti}_{0.10}$) alloy matrices, definition of peaks is better in the case of sample $\text{Sn}_{0.70}\text{Ni}_{0.20}\text{Ti}_{0.10}$ (Fig. 7b) as compared to $\text{Sn}_{0.60}\text{Ni}_{0.25}\text{Ti}_{0.15}$ (Fig. 7a). Hence, it can be expected that (de)intercalation of the Li into $\text{Sn}_{0.70}\text{Ni}_{0.20}\text{Ti}_{0.10}$ alloy matrix is more favorable and confirms the nano-grains Sn impregnated into the inactive alloy matrix for the good electrochemical performance as discussed in the subsequent section.

3.4. Charge-discharge studies on SnNiTi and Sn-NiTi alloy matrices

For the eventual application of anode matrices thus synthesized, characterization through galvanostatic charge-discharge studies at 30 mA g^{-1} in the voltage range $0.005 - 2 \text{ V}$ for 50 cycles are significant (Figs. 8, 9). Voltage vs capacity profile clearly shows the pronounced voltage profile and increased charge-discharge capacity for the composition $\text{Sn}_{0.70}\text{Ni}_{0.20}\text{Ti}_{0.10}$ alloy matrix (Fig. 8b) as compared to $\text{Sn}_{0.60}\text{Ni}_{0.25}\text{Ti}_{0.15}$ (Fig. 8a). This is in good agreement with the CV results for the nano-grains of Sn impregnated into the NiTi inactive alloy matrix during cycling. Also, the initial discharge/charge capacities for compositions $\text{Sn}_{0.60}\text{Ni}_{0.25}\text{Ti}_{0.15}$ and $\text{Sn}_{0.70}\text{Ni}_{0.20}\text{Ti}_{0.10}$ of the alloy matrix were found to be $482/412 \text{ mAh g}^{-1}$ and $700/566 \text{ mAh g}^{-1}$ respectively. From these, we have a typical composition $\text{Sn}_{0.70}\text{Ni}_{0.20}\text{Ti}_{0.10}$ alloy matrix delivered the good charge capacity of 566 mAh g^{-1} in the voltage range $0.005 - 2 \text{ V}$ in the 1st cycle (Fig. 8b). It can also be seen that voltage drop and polarization of Li vs $\text{Sn}_{0.70}\text{Ni}_{0.20}\text{Ti}_{0.10}$ cell at 50th cycle was less compared with Li vs $\text{Sn}_{0.60}\text{Ni}_{0.25}\text{Ti}_{0.15}$ for the same 50th cycle as depicted in Fig. 8a-b. Also, the galvanostatic cycling stability of the Li cells with the composition $\text{Sn}_{0.60}\text{Ni}_{0.25}\text{Ti}_{0.15}$ and $\text{Sn}_{0.70}\text{Ni}_{0.20}\text{Ti}_{0.10}$ through the mill-heat process are shown in Fig. 9. In terms of stability results, it can be seen that alloy matrix composition corresponding to $\text{Sn}_{0.70}\text{Ni}_{0.20}\text{Ti}_{0.10}$ yielded remarkable capacity coupled with good capacity retention results during cycling 1-50th cycle as depicted in Fig. 9. Cycle performance details of the high performance $\text{Sn}_{0.70}\text{Ni}_{0.20}\text{Ti}_{0.10}$ alloy matrix anode can be summarized as the initial discharge/charge capacity ($700/566 \text{ mAh g}^{-1}$) which showed large irreversible capacity 134 mAh g^{-1} ($\sim 19\%$). But this drop could be reduced from the second cycle onwards (discharge/charge capacity, $573/518 \text{ mAh g}^{-1}$) the irreversible capacity is reduced to 55 mAh g^{-1} ($\sim 9\%$). Of these two alloy matrix compositions $\text{Sn}_{0.60}\text{Ni}_{0.25}\text{Ti}_{0.15}$ and $\text{Sn}_{0.70}\text{Ni}_{0.20}\text{Ti}_{0.10}$, the latter yielded higher capacity. For this reason, rate

capability studies at 60 mA g^{-1} and 90 mA g^{-1} have also been investigated for the Li vs $\text{Sn}_{0.70}\text{Ni}_{0.20}\text{Ti}_{0.10}$ cell. However, there seems to be marked capacity fade at these rates for the alloy matrix sample with the composition $\text{Sn}_{0.70}\text{Ni}_{0.20}\text{Ti}_{0.10}$. The pronounced drop observed during the starting of the lithiation process in the 1st cycle can be attributed to traces of Ni_3Sn_4 phase and traces of oxides formed during milling leading to irreversible capacity because Li cannot be extracted from Li_2O during electrochemical reactions.^{33,41}

3.5. Flexibility of anode active site *versus* Poisson ratio during Li (de)intercalation

The Li^+ ion species generated during the course of cycling have to be essentially accommodated on active metallic site(s) M of anode through intercalation ($\text{Li}_{4.4}\text{M}$, M = Si, Sn) process.^{22,42} Invariably this necessitates suitable space to accommodate the intercalated Li species followed by restoring to original size of the active site upon de-intercalation. This implies imperative requirement on flexibility for the active site. Another daunting issue that needs to be addressed is wearing out of electronic contact between particles and the current collector in the charge-discharge cycles. It turns out that in the design of suitable anode based on active and inactive site concept the choices have to be necessarily between either Si or Sn (M = Si, Sn). As outlined earlier Sn as the active site has an edge over the Si. Furthermore, the concept of the Poisson ratio ν (describing the ratio of flexibilities in the lateral versus longitudinal directions) can be invoked for this system.³⁵⁻³⁶ Comparing the elastic properties in particular Poisson's ratio of metals *viz.*, Si ($\nu_{\text{Si}} = 0.17$), Sn ($\nu_{\text{Sn}} = 0.33$), Ni ($\nu_{\text{Ni}} = 0.3$) and Ti ($\nu_{\text{Ti}} = 0.305$) the Sn-NiTi alloy matrix system suggests a clear advantage in terms of flexibility to accommodate Li^+ ions during cycling in contrast to Si based system having lower Poisson ratio $\nu_{\text{Si}} = 0.17$ which is only half of the NiTi alloy matrix ($\nu_{\text{Ni}} = 0.3$, $\nu_{\text{Ti}} = 0.305$). Unique advantages of NiTi alloy matrix exhibiting super-elasticity (with the respective Poisson ratio being quite

comparable to Sn) characteristics is that it can absorb large stress coming from the mammoth volume expansion of the active Sn site upon intercalation. The NiTi alloy is found to be an appropriate second phase alloy matrix and also being inactive with Sn³²⁻³³ which is excellent flexibility features can be schematized as in Fig. 10. Obviously, Sn species having two fold higher value of Poisson ratio stands better placed as active site to accommodate the intercalated Li⁺ ions over the Si.³⁵⁻³⁶ Hence, it is reasonable to generalize that the Sn-NiTi alloy matrix exhibiting a superior long term cycling to accommodate Li⁺ ions during (de)intercalation process (Sn ↔ Li_{4.4}Sn) has clear advantage to ensure electronic contact and structural stability coupled with superior electrochemical performance.

3.6. High voltage (> 4.2 V) Li-ion pouch cell: features and performance

Considering the forgoing salient features of the anode system in the Li cells of the present study and also the extensive application scope of this anode system reported³²⁻³³ it is much worthwhile to employ this anode in the design of Li-ion pouch cell having clear distinct advantages *viz.*, light weight, low cost, high energy density. Eventually, this might facilitate application of this Li-ion pouch cell in most preferred for EVs and HEVs applications over other type of Li-ion cells.⁴³ Accordingly, high energy storage Li-ion pouch cell fabricated in our lab with rolling in smart-design employing Sn_{0.70}Ni_{0.20}Ti_{0.10} anode and LNi_{1/3}Mn_{1/3}Co_{1/3}O₂:LNi_{0.5}Mn_{0.5}O₂ cathode with rated a capacity scale of ~ 500 mAh (Figs. 9a, 10a). After an aging of 24 h, the open circuit voltage of the Li-ion pouch cell was measured at 0.652 V (Fig. 11a). This OCV is higher than the earlier reports on OCV of Li-ion pouch cell with mesocarbon microbeads (MCMB) anode.⁴⁴ Turning to the electrochemical performance of Li-ion pouch cell, it is essential to pass through the initial-formation cycle at 30 mA (constant current) upto 4.6 V.⁴⁵ The initial-formation cycle (at 30 mA) and cycling performance (at 50

mA) of Li-ion pouch cell is shown in Fig. 11b (voltage vs time, current vs time). Also it is important to scrutinize the performance of voltage vs cell capacity of this Li-ion pouch cell having immense futuristic application scope (Fig. 11c). To assess the cycling stability of the Li-ion pouch cell fabricated in our lab studies were extended to evaluate cell capacity in the voltage range 3 - 4.6 V up to 100 cycles (at 50 mA) as given in Fig. 11d.

From this charge-discharge study, we have that the Li-ion pouch cell delivered a discharge capacity of ~ 500 mAh at 11th cycle in the voltage range 3 to 4.6 V and also it is found that the capacity fade is similar to that of the Li cell (Li vs Sn_{0.70}Ni_{0.20}Ti_{0.10}). In order to demonstrate the application of the thus designed Li-ion pouch cell cycle studies were limited to 100 cycles. It is significant to note that even after 100 cycles, there is no change in the dimension, geometry of the Li-ion pouch cell as depicted in Fig. 12a and also the open circuit voltage under charged state was found to be 4.57 V (Fig. 12b). In order to demonstrate the usefulness of the Li-ion pouch cell in actual applications, this cell was used for running a toy-car with a load 1.1 Wh on a slanted flooring (Fig. 12c) and also on a coarse bitumen road (Fig. 12d,e) in CSIR-CECRI, India (*video demonstration for Li-ion pouch cell in supplementary S¹*). During this demonstration, running of the electronic toy-car consumed current at the rate of 315 mA. The high voltage (> 4.2 V) Li-ion pouch cell realized may form the basis to merit application in futuristic energy storage systems for the EVs and HEVs.

4. Conclusions

Well characterized nano-granular Sn impregnated inactive NiTi alloy matrix anode has been synthesized through a more feasible *mill-heat* method. Poly crystalline grains of Sn in NiTi alloy matrix revealed an average size of ~ 25 nm as suitable anode materials for Li-ion batteries. This Sn active site(s) matrix anode serving as host for intercalated lithium species has several

clear advantages *viz.*, better electronic properties, favorable elastic features in particular Poisson ratio akin to the host Sn-NiTi matrix and cycling stability facilitating EV, HEV applications. Li cell assembled using this optimized alloy matrix anode (Li vs $\text{Sn}_{0.70}\text{Ni}_{0.20}\text{Ti}_{0.10}$) delivered a charge capacity of 566 mAh g^{-1} (1st cycle) in the voltage range 0.005 – 2 V. The cell fabrication studies were further extended with the design of Li-ion pouch cell (rolling in smart-design) using this optimized alloy matrix anode ($\text{Sn}_{0.70}\text{Ni}_{0.20}\text{Ti}_{0.10}$) in conjunction with composite cathode ($\text{LNi}_{1/3}\text{Mn}_{1/3}\text{Co}_{1/3}\text{O}_2:\text{LNi}_{0.5}\text{Mn}_{0.5}\text{O}_2$, wt. % of 75:25). Smart-design Li-ion pouch cell fabricated yields an impressive high voltage of (4.2 V) with remarkable discharge capacity of $\sim 500 \text{ mAh}$ at 11th cycle in the voltage range 3 to 4.6 V coupled with cycling performance can be attributed to the unique combination of alloy matrix anode versus composite cathode. Furthermore, the demonstration of running a toy-car with a load 1.1 Wh on a coarse bitumen road in CSIR-CECRI (India) testifies the successful design of durable high voltage Li-ion batteries in near future.

Supporting Information

Video demonstration for Li-ion pouch cell ([S¹](#)).

Acknowledgments

The first author, P. Manikandan, acknowledges the Council of Scientific and Industrial Research (CSIR), New Delhi for granting the financial support for the above work in the form of a senior research fellowship and also our thanks to the Director, CSIR-CECRI, Karaikudi.

References

- 1 M. Armand and J.M. Tarascon, *Nature*, 2008, **451**, 652–657.
- 2 M. Whittingham, *Chem. Rev.* 2004, **104**, 4271–4301.
- 3 J. Tarascon and M. Armand, *Nature*, 2001, **414**, 359–367.

- 4 A.S. Arico, P. Bruce, B. Scrosati, J.M. Tarascon and W.V. Schalkwijk, *Nat. Mater.* 2005, **4**, 366–377.
- 5 J.B. Goodenough and Y. Kim, *Chem. Mat.* 2010, **22**, 587–603.
- 6 B. Song, H. Liu, Z. Liu, P. Xiao, M.O. Lai and L. Lu., *Scientific Reports* DOI: 10.1038/srep03094.
- 7 M.M. Thackeray, S. Kang, C.S. Johnson, J.T. Vaughey, R. Benedek and S.A. Hackney, *J. Mater. Chem.*, 2007, **17**, 3112–3125.
- 8 W. He, J. Qian, Y. Cao, X. Ai and H. Yang, *RSC Advances*, 2012, **2**, 3423–3429.
- 9 K. Mizushima, P.C. Jones, P.J. Wiseman and J.B. Goodenough, *Mater. Res. Bull.*, 1980, **15**, 783–789.
- 10 J.N. Reimers and J.R. Dahn, *J. Electrochem. Soc.*, 1992, **139**, 2091–2097.
- 11 Z. Lu, D.D. MacNeil and J.R. Dahn, *Electrochem. Solid-State Lett.*, 2001, **4**, A200–A203.
- 12 D. MacNeil, Z. Lu and J.R. Dahn, *J. Electrochem. Soc.*, 2002, **149**, A1332–A1336.
- 13 Y.K. Sun, S.T. Myung, H.J. Bang, B.C. Park, S.J. Park and N.Y. Sung, *J. Electrochem. Soc.*, 2007, **154**, A937–A942.
- 14 A.S. Prakash, P. Manikandan, K. Ramesha, M. Sathiya, J.M. Tarascon and A.K. Shukla, *Chem. Mater.*, 2010, **22**, 2857–2863.
- 15 H. Zhang, X.P. Gao, G.R. Li, T.Y. Yan and H.Y. Zhu, *Electrochimica Acta*, 2008, **53**, 7061–7068.
- 16 G.P. Kim, S. Park, I. Nam, J. Park and J. Yi, *J. Mater. Chem A*, 2013, **1**, 3872–3876.
- 17 J.O. Besenhard, J. Yang and M. Winter, *J. Power Sources*, 1997, **68**, 87–90.
- 18 P. Bruce, B. Scrosati and J.M. Tarascon, *Angew. Chem. Int. Ed.*, 2008, **47**, 2930–2946.
- 19 P. Gu, R. Cai, Y. Zhou and Z. Shao, *Electrochim. Acta*, 2010, **55**, 3876–3883.

- 20 O. Mao, R.A. Dunlap and J.R. Dahn, *J. Electrochem. Soc.*, 1999, 146, **405**–413.
- 21 S. Chen, P. Chen, M. Wu, D. Pan and Y. Wang, *Electrochem. Commun.*, 2010, **12**, 1302–1306.
- 22 R. Hu, H. Liu, M. Zeng, H. Wang and M. Zhu, *J. Power Sources*, 2011, **21**, 4629–4635.
- 23 H. Guo, H. Zhao and X. Jia, *Electrochem. Comm.*, 2007, **9**, 2207–2211.
- 24 G.F. Ortiz, R. Alcantara, I. Rodriguez and J.L. Tirado, *J. Electroanal. Chem.*, 2007, **605**, 98–108.
- 25 Z. Chen, J. Qian, X. Ai, Y. Cao and H. Yang, *J. Power Sources*, 2009, **189**, 730–732.
- 26 W.M. Zhang, J.S. Hu, Y.G. Guo, S.F. Zheng, L.S. Zhong, W.G. Song and L.J. Wan, *Adv. Mater.*, 2008, **20**, 1160–1165.
- 27 C.M. Park, W.S. Chang, H.C. Jung, J.H. Kim and H.J. Sohn, *Electrochem. Commun.*, 2009, **11**, 2165–2168.
- 28 G.X. Wang, J.H. Ahn, M.J. Lindsay, L. Sun, D.H. Bradhurst, S.X. Dou and H.K. Liu, *J. Power Sources*, 2001, **97–98**, 211–215.
- 29 J. Hassoun, G. Mulas, S. Panero and B. Scrosati, *Electrochem. Commun.*, 2007, **9**, 2075–2081.
- 30 G.X. Wang, B. Wang, X.L. Wang, J.S. Park, S.X. Dou, H. Ahn and K. Kim, *J. Mater. Chem.*, 2009, **19**, 8378–8384.
- 31 H. Jung, Y.U. Kim, M.S. Sung, Y. Hwa, G. Jeong, G.B. Kim and H.J. Sohn, *J. Mater. Chem.*, 2011, **21**, 11213–11216.
- 32 R. Hu, H. Liu, M. Zeng, J. Liu and M. Zhu, *J. Mater. Chem.*, 2012, **22**, 9539–9545.
- 33 R. Hu, H. Liu, M. Zeng, J. Liu and M. Zhu, *J. Power Sources*, 2013, **244**, 456–462.
- 34 X.L. Wang and W.Q. Han, *ACS Appl. Mat. Interfaces*, 2010, **2**, 3709–3713.

- 35 C.Y. Chou, H. Kim and G.S. Hwang, *J. Phys. Chem. C*, 2011, **115**, 20018–20026.
- 36 M.E. Stournara, P.R. Guduru and V.B. Shenoy, *J. Power Sources*, 2012, **208**, 165–169.
- 37 M. Uno, K. Ogawa, Y. Takeda, Y. Sone, K. Tanaka, M. Mita and H. Saito, *J. Power Sources*, 2011, **196**, 8755–8763.
- 38 P. Manikandan, P. Periasamy and R. Jagannathan, *J. Power Sources*, 2014, **264**, 299–310.
- 39 X. Luo, X. Wang, L. Liao, S. Gamboa and P.J. Sebastian, *J. Power Sources*, 2006, **158**, 654–658.
- 40 R.Z. Hu, Y. Zhang and M. Zhu, *Electrochim. Acta*, 2008, **53**, 3377–3385.
- 41 S. Ohara, J. Suzuki, K. Sekine and T. Takamura, *J. Power Sources*, 2004, **136**, 303–306.
- 42 D. Wang, F. Li, G. Ping, D. Chen, M. Fan, L. Qin, L. Bai, G. Tian, C. Lu and K. Shu, *Int. J. Electrochem. Sci.*, 2013, **8**, 9618–9628.
- 43 K. Amine, I. Belharouak, Z. Chen, T. Tran, H. Yumamoto, N. Ota, S.T. Myung and Y.K. Sun, *Adv. Mater.*, 2010, **22**, 3052–3057.
- 44 P. Manikandan, P. Periasamy and R. Jagannathan, *J. Power Sources*, 2014, **245**, 501–509.
- 45 S.S. Zhang, *J. Power Sources*, 2006, **161**, 1385–1391.

Figure 1

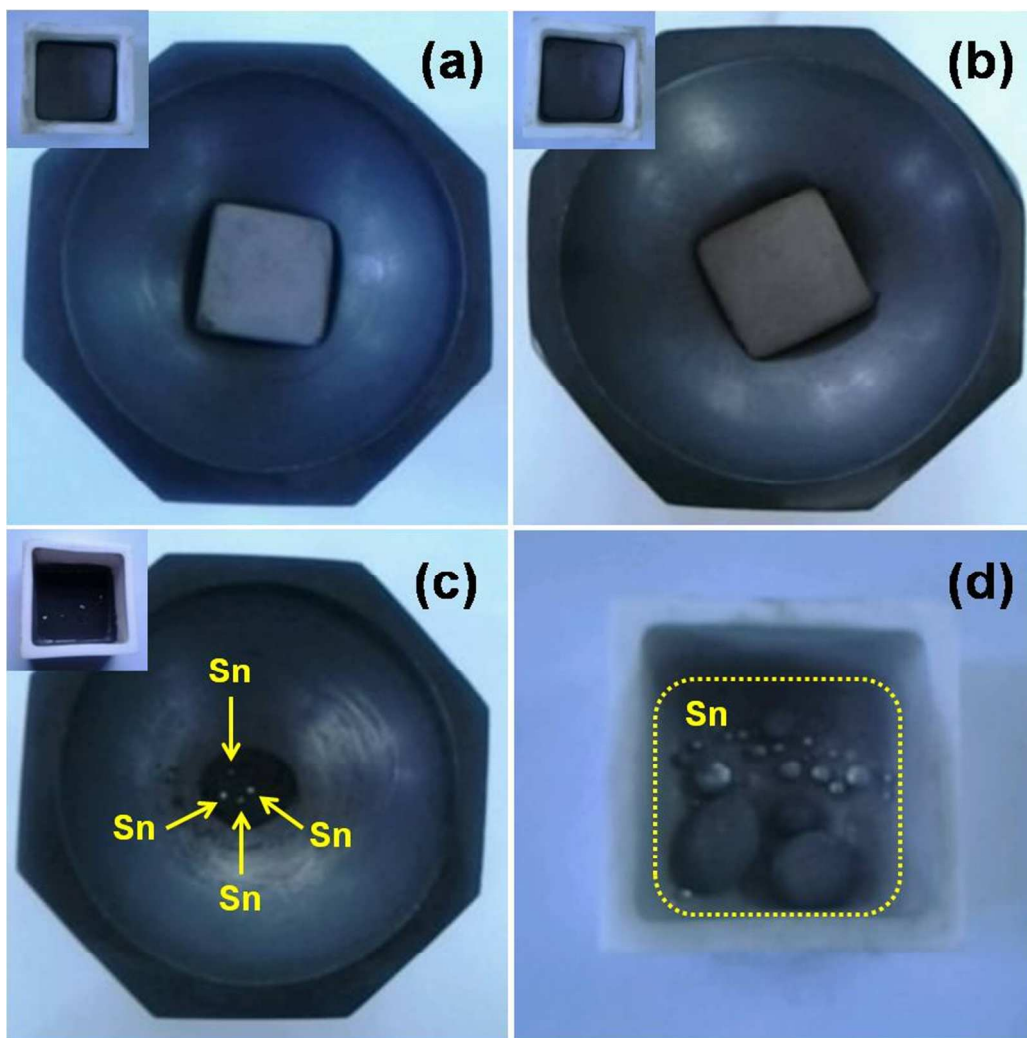


Fig. 1 Photographs depicting images of the as-synthesized alloy matrix samples as obtained from the furnace placed in agate mortar/ceramics boat having the compositions with relative wt. %: (a) $\text{Sn}_{0.60}\text{Ni}_{0.25}\text{Ti}_{0.15}$ (60:25:15); (b) $\text{Sn}_{0.70}\text{Ni}_{0.20}\text{Ti}_{0.10}$ (70:20:10); (c) $\text{Sn}_{0.80}\text{Ni}_{0.15}\text{Ti}_{0.05}$ (80:15:05) and (d) 100:00:00 ($\text{Sn}_{1.00}\text{Ni}_{0.00}\text{Ti}_{0.00}$) through mill-heat process. Segregation of Sn particles can be clearly seen in photographs (c) and (d).

Figure 2

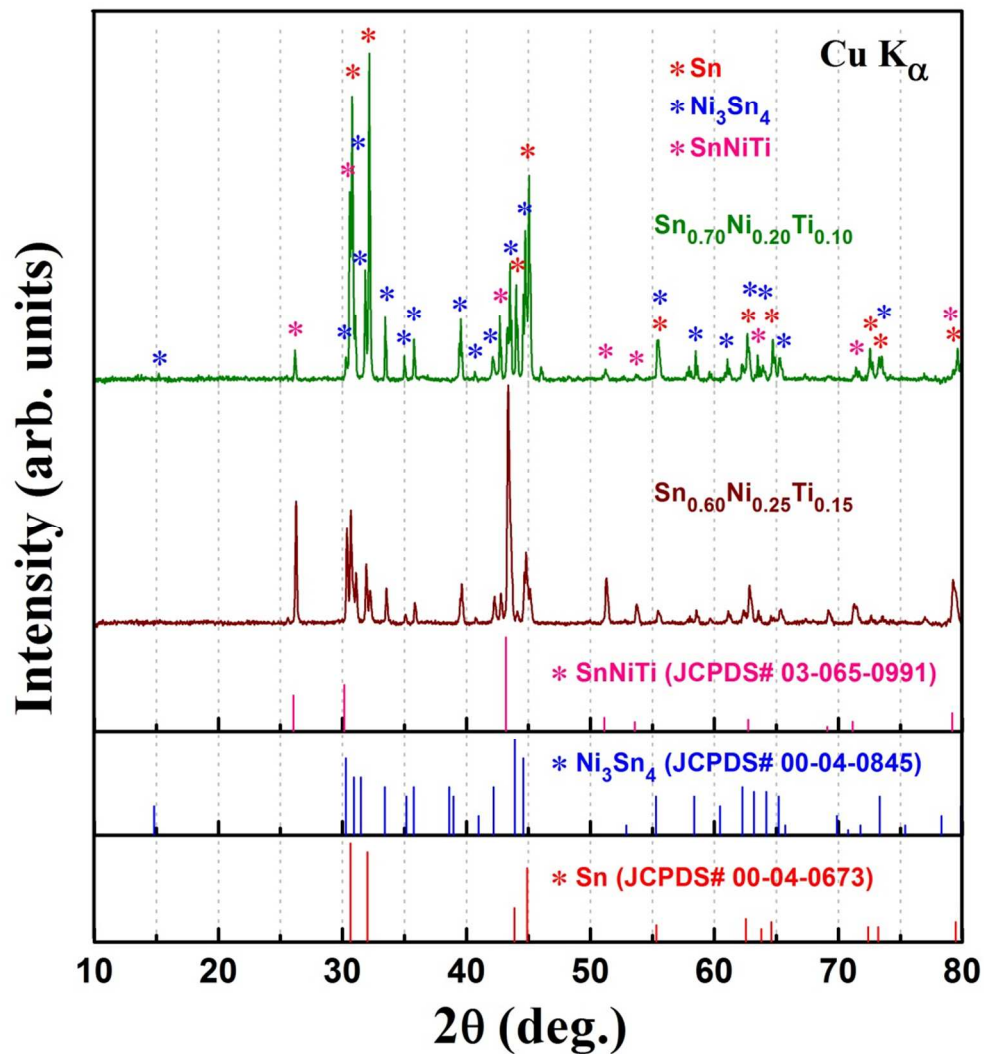


Fig. 2 Powder X-ray diffraction patterns of alloy matrix synthesized through mill-heat process in Ar (at 900 °C for 12 h) compared with standard patterns Sn (JCPDS# 00-04-0673), Ni_3Sn_4 (JCPDS# 00-04-0845), SnNiTi (JCPDS# 03-065-0991), $\text{Sn}_{0.60}\text{Ni}_{0.25}\text{Ti}_{0.15}$ and $\text{Sn}_{0.70}\text{Ni}_{0.20}\text{Ti}_{0.10}$ composition.

Figure 3

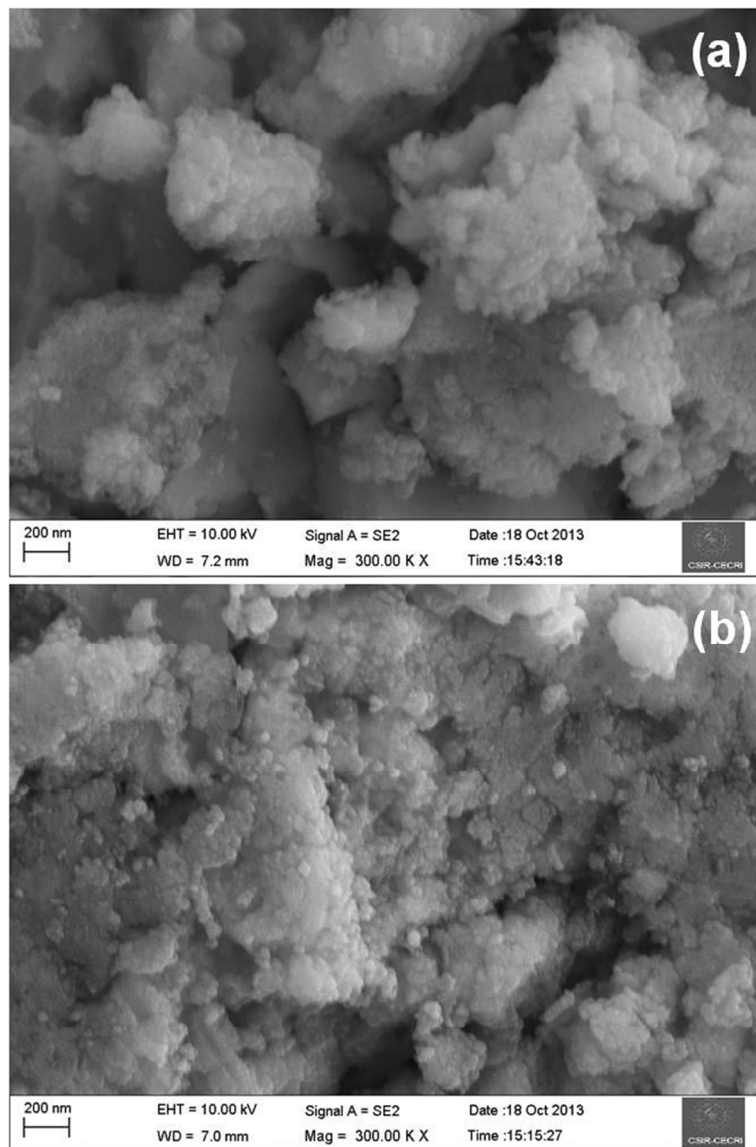


Fig. 3 Particle morphology micrographs using FE-SEM for alloy matrix with the composition:

(a) $\text{Sn}_{0.60}\text{Ni}_{0.25}\text{Ti}_{0.15}$ and (b) $\text{Sn}_{0.70}\text{Ni}_{0.20}\text{Ti}_{0.10}$.

Figure 4

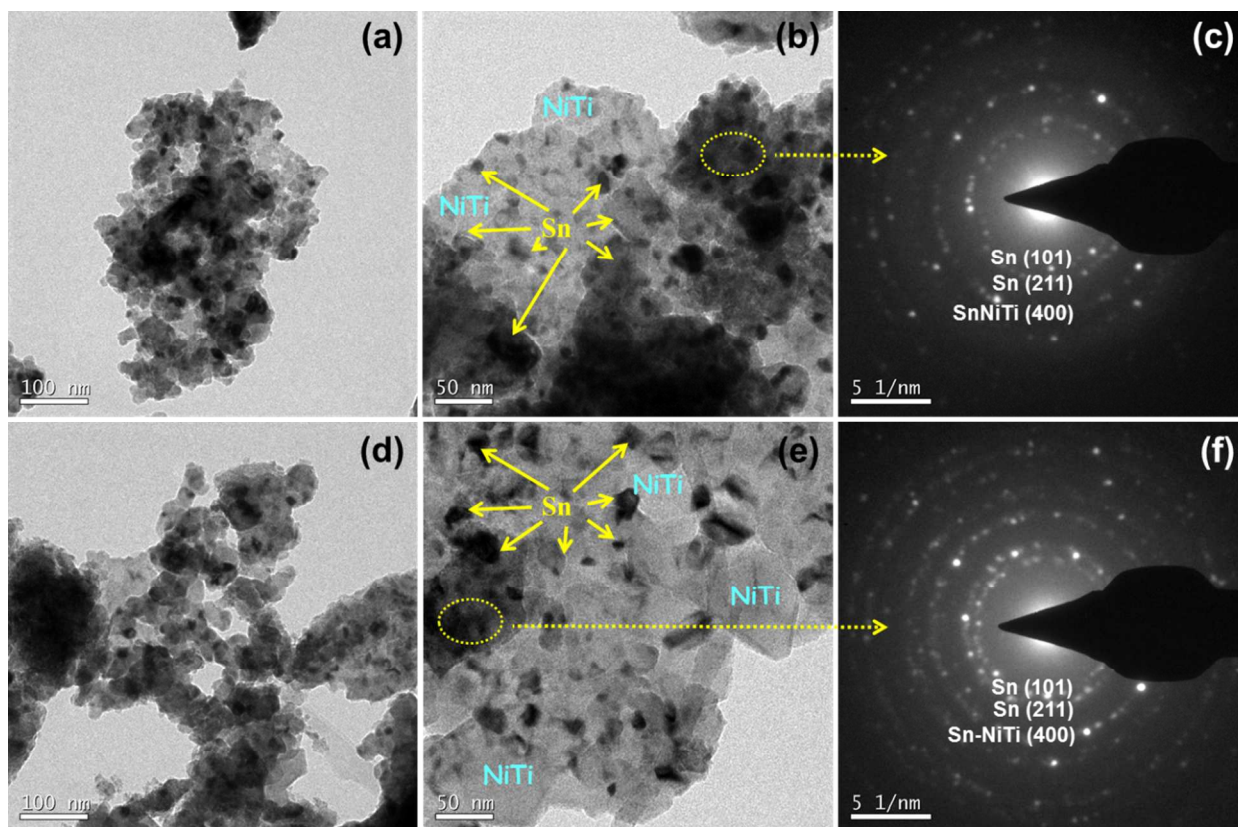


Fig. 4 Particle morphology micrographs and corresponding SAED patterns using TEM for alloy matrix with the composition: (a-c) $\text{Sn}_{0.60}\text{Ni}_{0.25}\text{Ti}_{0.15}$ and (d-f) $\text{Sn}_{0.70}\text{Ni}_{0.20}\text{Ti}_{0.10}$.

Figure 5

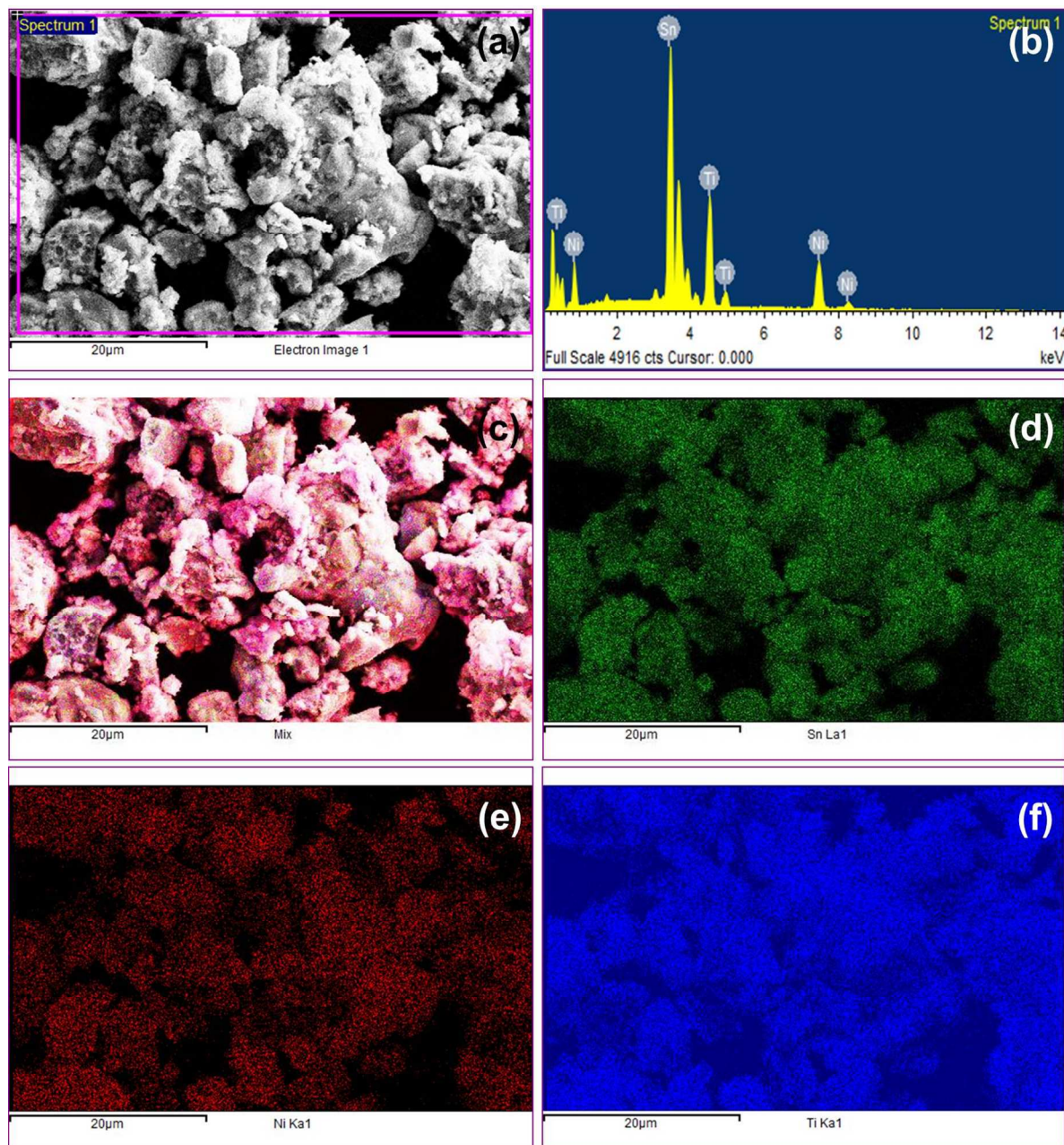


Fig. 5 The FE-SEM elemental mapping images of alloy matrix with the composition $\text{Sn}_{0.60}\text{Ni}_{0.25}\text{Ti}_{0.15}$ (a) FE-SEM image corresponding to the quantified area, (b) energy dispersive X-ray analysis, (c) simultaneous occurrence of elements, (d) Sn in green, (e) Ni in red and (f) Ti in blue colors.

Figure 6

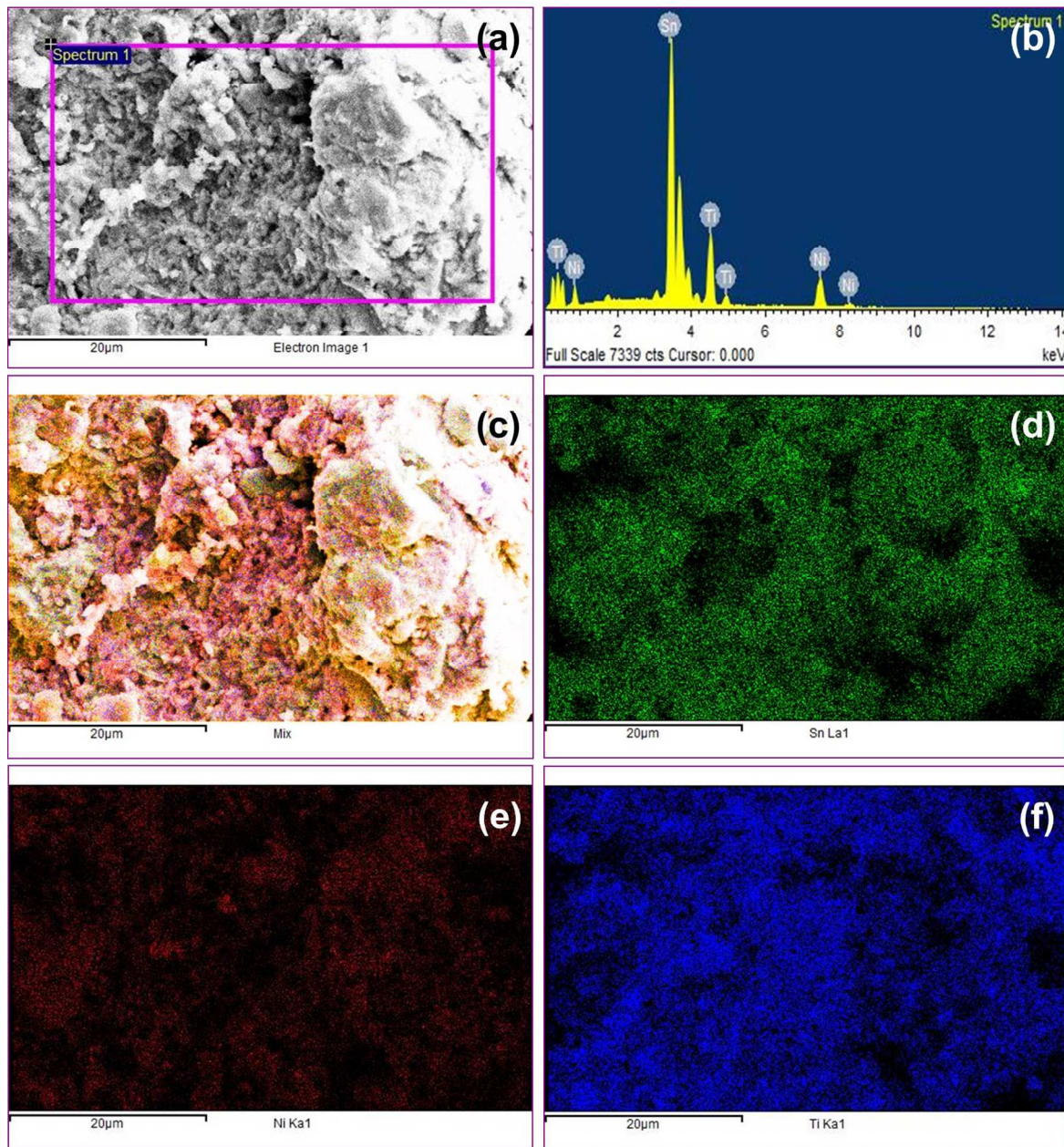


Fig. 6 The FE-SEM elemental mapping images of alloy matrix with the composition $\text{Sn}_{0.70}\text{Ni}_{0.20}\text{Ti}_{0.10}$ (a) FE-SEM image corresponding to the quantified area, (b) energy dispersive X-ray analysis, (c) simultaneous occurrence of elements, (d) Sn in green, (e) Ni in red and (f) Ti in blue colors.

Figure 7

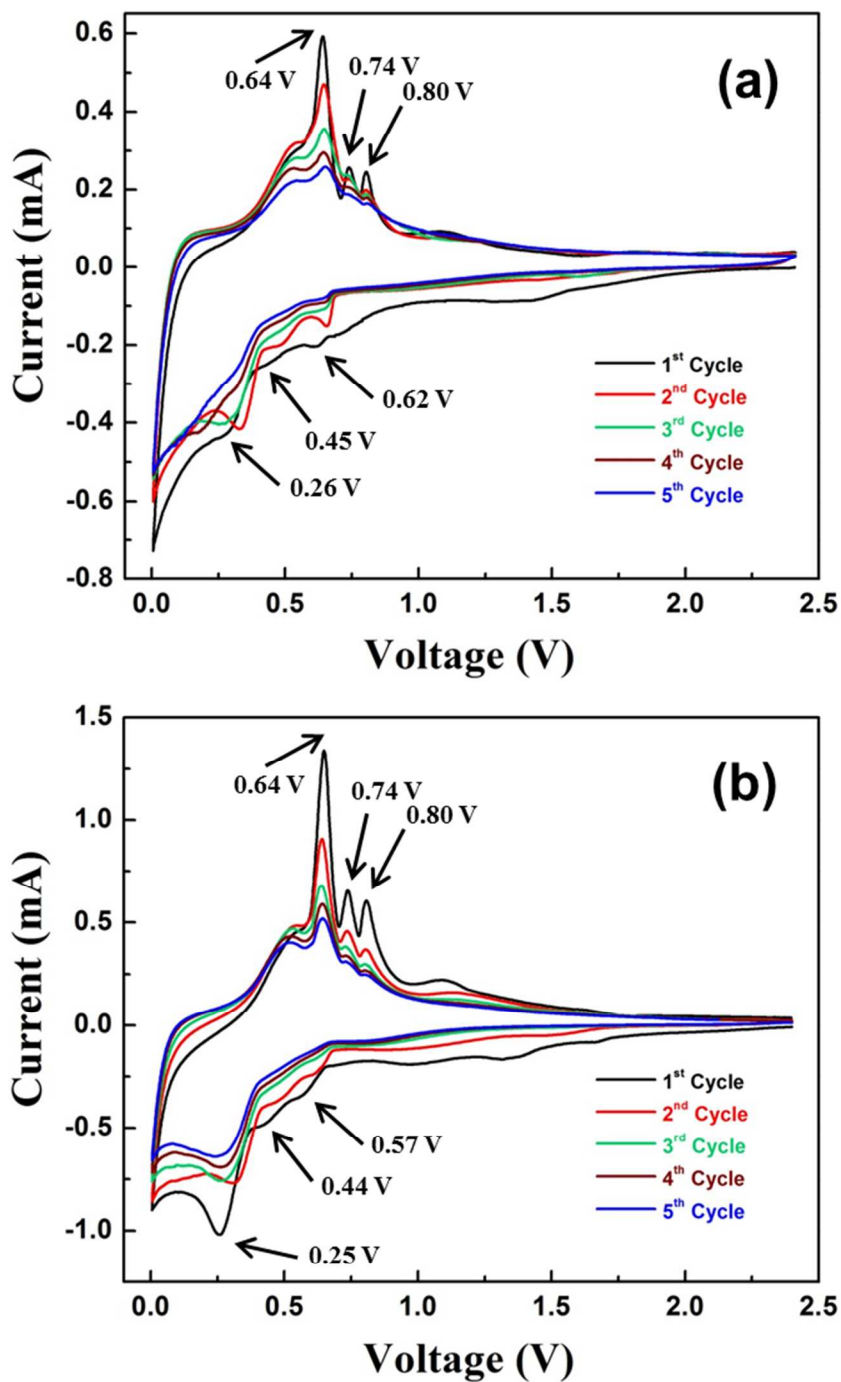


Fig. 7 Cyclic voltammograms of lithium cells made with the alloy matrix (a) Li vs Sn_{0.60}Ni_{0.25}Ti_{0.15}, (b) Li vs Sn_{0.70}Ni_{0.20}Ti_{0.10} in the voltage range from 0.005 to 2.4 V (1st – 5th cycles) at 0.1 mV s⁻¹ (1 M LiPF₆ in 1:1 EC–DMC solvents).

Figure 8

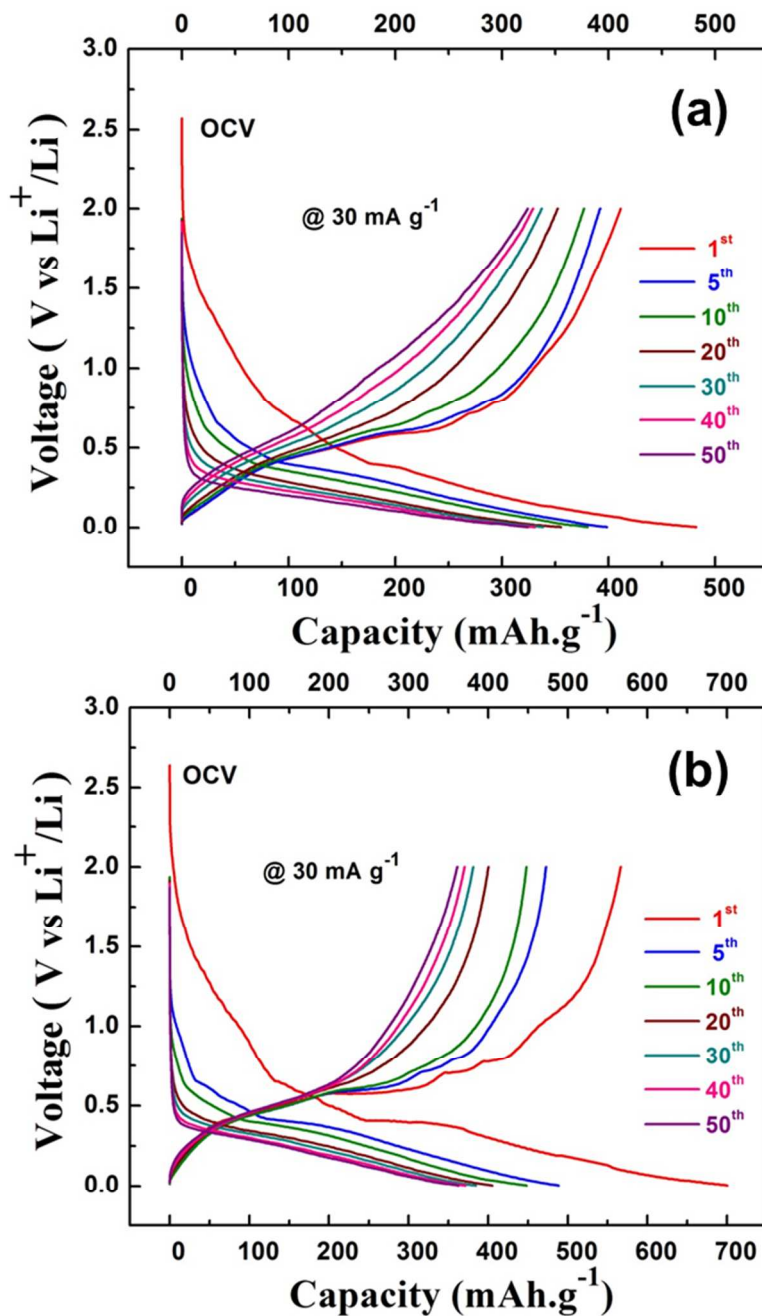


Fig. 8 Voltage vs capacity profile of lithium cells made with the alloy matrix (a) Li vs $\text{Sn}_{0.60}\text{Ni}_{0.25}\text{Ti}_{0.15}$, (b) Li vs $\text{Sn}_{0.70}\text{Ni}_{0.20}\text{Ti}_{0.10}$ in the voltage range from 0.005 - 2 V (1– 50 cycles) at 30 mA.g^{-1} (1 M LiPF_6 in 1:1 EC–DMC solvents).

Figure 9

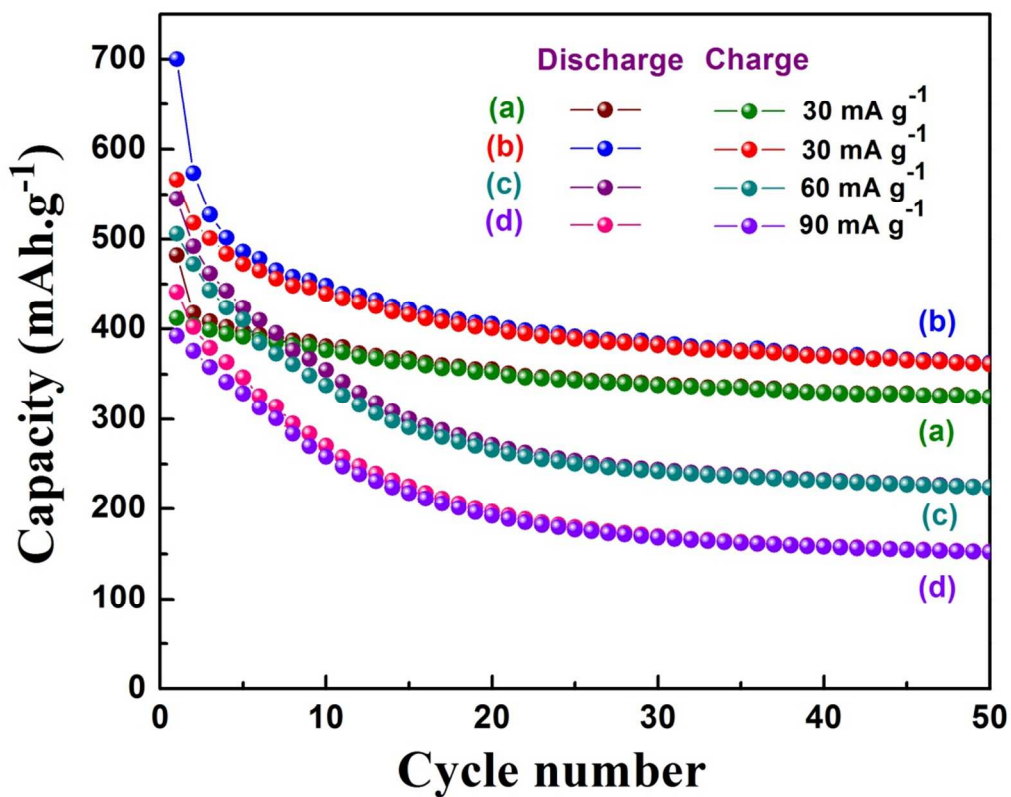


Fig. 9 Charge-discharge studies of lithium cells made with the alloy matrix (a) Li vs Sn_{0.60}Ni_{0.25}Ti_{0.15} at 30 mA g⁻¹, (b) Li vs Sn_{0.70}Ni_{0.20}Ti_{0.10} at 30 mA g⁻¹, (c) Li vs Sn_{0.70}Ni_{0.20}Ti_{0.10} at 60 mA g⁻¹ and (d) Li vs Sn_{0.70}Ni_{0.20}Ti_{0.10} at 90 mA g⁻¹ in the voltage range from 0.005 - 2 V (1–50 cycles) at 30 mA g⁻¹ (1 M LiPF₆ in 1:1 EC–DMC solvents).

Figure 10

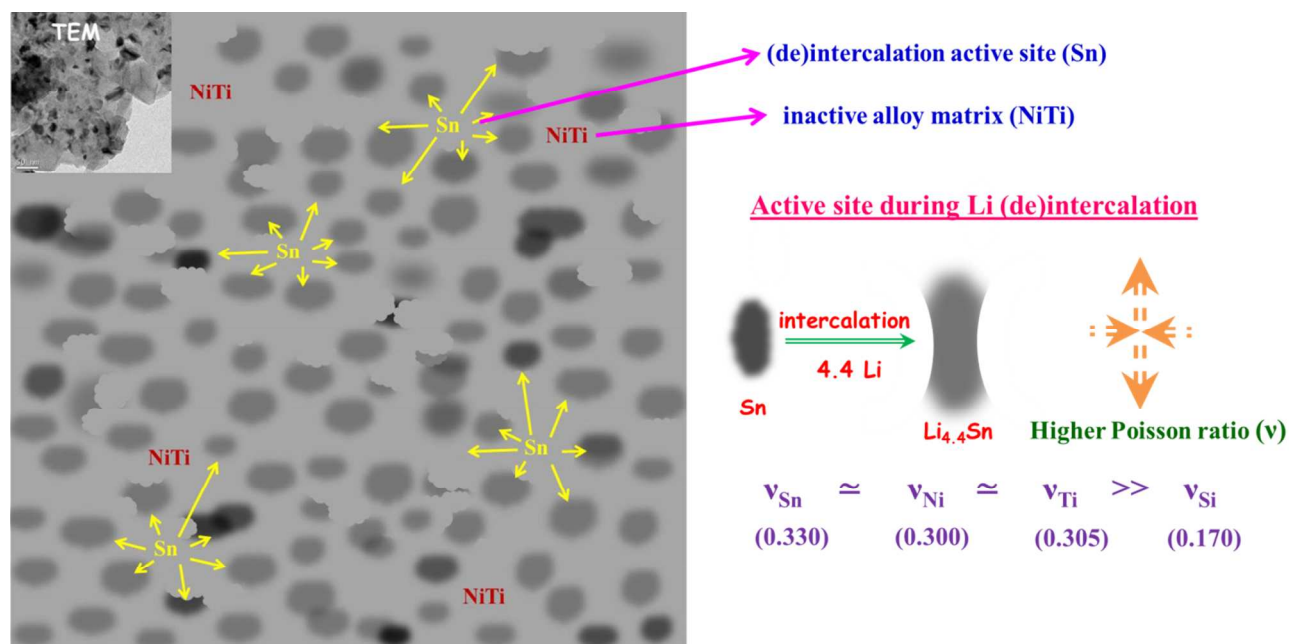


Fig. 10 Schematics illustrating the active Sn site and its expansion upon intercalation of Li^+ distributed over inactive NiTi matrix (explained on the basis of Poisson ration consideration) with the particle morphology in the inset using TEM.

Figure 11

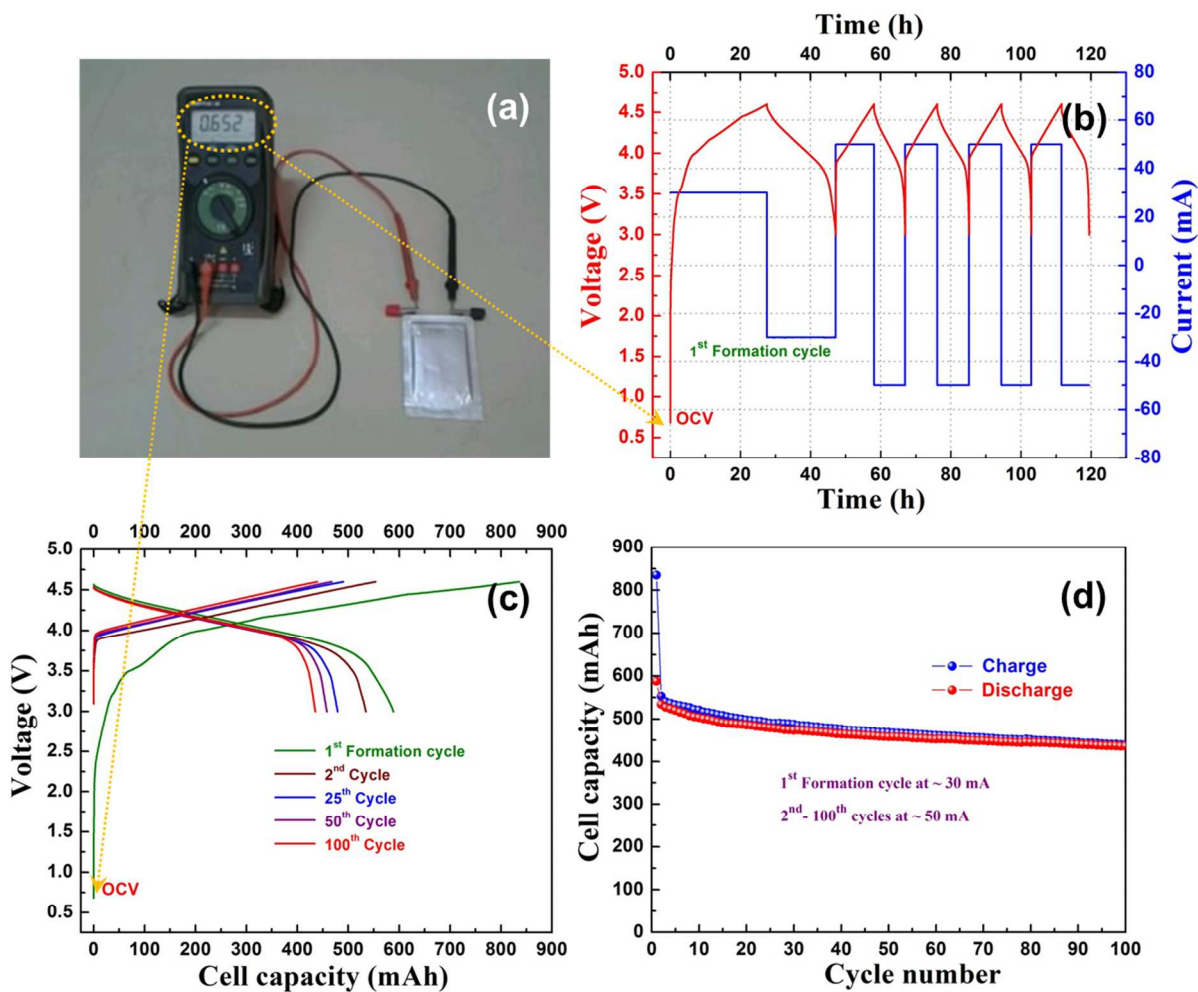


Fig. 11 The fabricated Li-ion pouch cell rolling in smart design (a) after an aging of 24 h the open circuit voltage measured at 0.652 V, (b) cycling performance corresponds to voltage vs time/current vs time, (c) voltage vs cell capacity and (d) cell capacity vs cycle number in the voltage range from 3 - 4.6 V (initial-formation cycle at 30 mA) and cycling performance at 50 mA for 2nd cycle onwards).

Figure 12

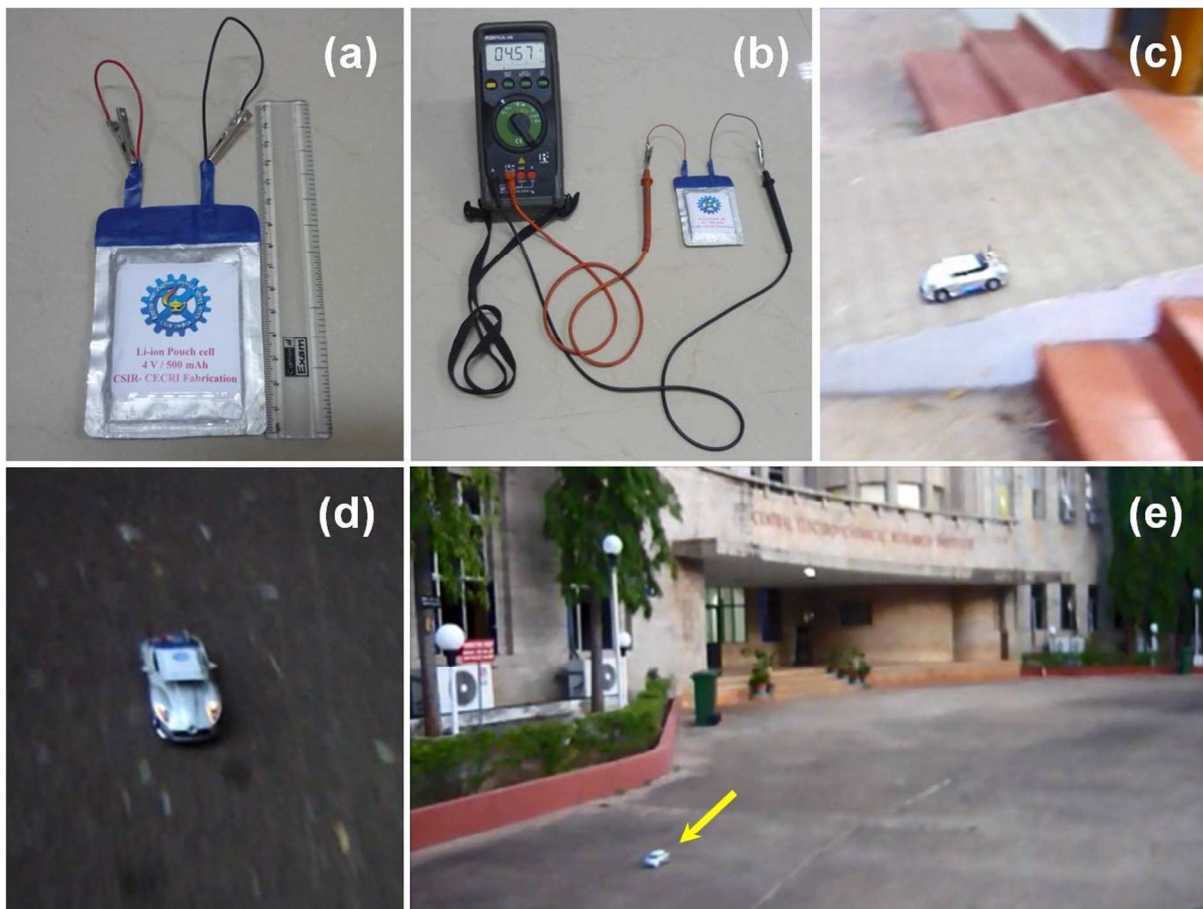


Fig. 12 Li-ion pouch cell features and performance: photographs illustrating the (a) fabricated Li-ion pouch cell rolling in smart design (500 mAh); (b) after 100 cycles, the open circuit voltage measured at 4.57 V under charged state; (c) the usefulness of the Li-ion pouch cell in demonstration of running a toy-car with a load 1.1 Wh on a slanted flooring and (d,e) in coarse bitumen road indicated using yellow arrow at CSIR-CECRI, India

Graphical abstract

Schematics illustrating flexibility of active Sn site(s) (with high Poisson ratio) accommodating Li^+ species.

